JOURNAL OF PROPULSION AND POWER
Vol. 19, No. 2, March–April 2003

Numerical Simulations of Wall and Shear Layer Instabilities in Cold Flow Setup

Jérôme Vétel,[*] Frédéric Plourde,[†] and Son Doan Kim[‡]
LET/ENSMA, 86961 Futuroscope Cedex, France
and
Jean-François Guery[§]
SNPE, Centre de Recherche du Bouchet, 91710 Vert-le-Petit, France

Experimental and numerical investigations were performed to characterize the potential sources of unstable behavior in a confined chamber that was both bounded by injecting walls and contained an emerging obstacle. The effect of the vortex shedding occurring in the wake of the obstacle and the wall vortex shedding phenomenon are described. The latter was found to be the most important source of acoustic energy in the chamber, and both experimental and numerical results demonstrated the interaction of pressure waves with vortex development. In addition, turbulent computations were performed to improve numerical results with regard to the experimental ones. Different levels of the pseudoinjected turbulence at the porous walls were also investigated, and such boundary conditions were found to affect strongly the unstable nature of the internal flowfield.

Nomenclature

a = speed of sound, m/s
E^* = total energy per unit of mass, $[p/\rho(\gamma - 1) + (v_i^2/2) + q^2]$, J/kg
$\boldsymbol{F}$ = convective flux vector
f_{nL} = nth longitudinal acoustic mode, $na/2L$, Hz
h_c = channel height, m
It = turbulence intensity, $\sqrt{(\overline{u'^2} + \overline{v'^2})}/u_c$
$\boldsymbol{K}$ = turbulent source term vector
L = channel length, m
l = length between the obstacle location and the submerged nozzle, m
$\dot{m}$ = total mass flow rate, kg/s
$\dot{m}_w$ = mass flow rate per injecting surface unit, $\mathrm{kg/m^2s}$
$\boldsymbol{n}$ = normal vector
Pr = Prandtl number
p = pressure, Pa
p^* = turbulent pressure, $(p + \frac{2}{3}\rho q^2)$, Pa
$\boldsymbol{Q}$ = conservation vector of Navier–Stokes equations
q = turbulent velocity, m/s
Re_c = axial Reynolds number, $\rho u_c h_c/\mu$
Re_{ij} = Reynolds tensor
Re_w = injection Reynolds number, $\rho v_w h_c/\mu$
$R_{u'p'}$ = correlation coefficient of the pressure and the velocity fluctuations, $\overline{u'(t).p'(t + \tau)}/\sqrt{[\overline{u'(t)^2}]}\sqrt{[\overline{p'(t)^2}]}$
$S_{x'}$ = power spectral density normalized by rms x' fluctuations, Hz^{-1}
T = temperature of the flow, K
u = velocity in x direction, m/s
u_c = characteristic mean flow velocity, $\dot{m}/\rho w_c h_c$, m/s
v = velocity in y direction, m/s
v_i = velocity component in the ith direction
w_c = channel width, m
X, Y = axial and transverse axis normalized respectively by l and h_c
x, y = Cartesian coordinates
x_i = ith direction
γ = ratio of specific heat
λ_T = total thermal conductivity, W/mK
μ = dynamic viscosity, kg/ms
μ_T = total dynamic viscosity, $(\mu + \mu_t)$, kg/ms
μ_t = turbulent dynamic viscosity, $C_\mu \overline{\rho} q^2/\omega$, kg/ms
ρ = density, $\mathrm{kg/m^3}$
σ_w = injected turbulence ratio at the porous injecting wall, $\sqrt{(\overline{v_w'^2})}/v_w$
τ = time delay, s
Ω = vorticity, s^{-1}
ω = dissipation frequency, s^{-1}

Subscript

w = value at injecting wall

Superscripts

$'$ = unsteady component
$-$ = mean value

I. Introduction

SEGMENTED solid propellant rocket motor technology for large space launchers provokes numerous induced problems in the internal flow, such as low-frequency instabilities, thermal protection failure, and slag mass accumulation of aluminum in the rear end of the motor, to name a few. Knowledge of internal flow behavior and the characterization of fundamental mechanisms is of major importance in the treatment of these problems. For instance, unstable behavior was detected on Titan motors[1,2] and also observed for the Ariane 5 solid rocket motor.[3] Both are segmented, that is, three to seven propellant blocks constitute the motor, depending on the motor and version, and are mainly characterized by the presence of inhibitor rings. Under such conditions, classical stability calculations[4] based on the acoustic balance predict stable behavior. As stated by Vuillot,[5] the cause for such oscillations has been traced to the coupling of unstable shear layers of the internal flow with the acoustic modes of the chamber. The relevance of vortex

---

Received 29 March 2002; revision received 5 November 2002; accepted for publication 6 November 2002. Copyright © 2003 by the American Institute of Aeronautics and Astronautics, Inc. All rights reserved. Copies of this paper may be made for personal or internal use, on condition that the copier pay the $10.00 per-copy fee to the Copyright Clearance Center, Inc., 222 Rosewood Drive, Danvers, MA 01923; include the code 0748-4658/03 $10.00 in correspondence with the CCC.

[*] Scientist, Laboratoire d' Etudes Thermiques/Ecole Nationale Supérieure de Mécanique et d' Aérotechnique.

[†] Centre National de la Recherche Scientifique Researcher, Laboratoire d' Etudes Thermiques/Ecole Nationale Supérieure de Mécanique et d' Aérotechnique. Member AIAA.

[‡] Professor, Laboratoire d' Etudes Thermiques/ Ecole Nationale Supérieure de Mécanique et d' Aérotechnique.

[§] Head, Computational Fluid Dynamics Group. Member AIAA.

shedding for segmented geometries was clearly identified by Dunlap and Brown[6] and Brown et al.,[7] who demonstrated that vortex shedding acted as an additional source of acoustic energy in segmented solid propellant rocket motors. Their works were mainly based on cold-gas simulations of a scaled-down Titan booster and underlined that acoustic wave amplification reached a maximum when the characteristic vortex shedding frequency was close to an acoustic mode of the experimental setup.

In addition, many experimental works[8,9] were dedicated to the fundamental organization of the flow inside a bounded wall injection chamber without any geometric disparities. Transition from laminar to turbulent regime was also studied numerically.[10–12] Dunlap et al.[13] studied wall injection flows through a cold-gas setup and were the first to mention a possible unstable mechanism in the vicinity of the injecting walls. However, Lupoglazoff and Vuillot[14] were the first to present numerical simulations in a classical wall injection channel without geometric disturbances and to demonstrate the presence of a wall vortex shedding phenomenon; because the flow was generated in a confined chamber, vortices impinged on the rear end of the chamber, and initial matched up with the acoustics. Then, a second possible acoustic energy source was detected and is still today of fundamental interest. In fact, it states that no important sheared areas are needed to provide an unstable mechanism. The competing mechanisms of the obstacle vortex shedding and the wall instability were first presented through numerical simulations of fired motors by Traineau et al.[15] Avalon et al.[9] investigated the unstable behavior of wall injection flows and proposed a stability criterion. First, according to linear stability, the evolution level of perturbations requires sufficient chamber length to grow and reach an unstable level. Second, the characteristic hydrodynamic frequency must be close to an available acoustic mode. Finally, instabilities are favored when the longitudinal location at which instabilities develop coincides with an acoustic velocity antinode. Such criteria constitute a first and useful step in the understanding of coupling phenomena between acoustics and hydrodynamics. According to Dotson et al.,[16] who analyzed the response of the Titan IV solid rocket motor upgrade, this type of coupling was responsible for unstable flow development. The new design studied corresponds to a three-segment motor without an obstacle. These researchers proposed an acoustic feedback model to explain the high-pressure fluctuations in the motor, assuming that pressure oscillations measured during the firing test were caused by coupling between the motor's fundamental acoustic mode and vortices that shed near the cavity between the second and the third propellant blocks.

Under these conditions, there are two possible ways of unstable development in solid propellant rocket motors. First, the vortex shedding phenomenon occurring in an intense sheared area of the flow was mainly studied behind diaphragms and restrictors in cold-gas simulations and its coupling with the acoustics. Second, through numerical results, as well as stability analysis of test firing, the wall vortex shedding phenomenon was found to act no differently from its counterpart arising in a configuration without emerging obstacles. According to Zhao et al.[17] and Staab et al.,[18] the generation of a vorticity pattern may arise from an interaction between pressure gradient and injecting wall. Thus, from numerical investigations, the aim of this study is to detect the possible simultaneous existence of the two different unstable sources by studying the destabilization mechanisms of a segmented wall injection flow induced in a confined chamber with an emerging obstacle. The presence of such an obstacle may cause the development of a vortex shedding phenomenon in its wake. Subsequently, the behavior of the main flow and its possible interaction with the wall injection will be pointed out. The present work is divided as follows. First, the numerical computations are presented. Calculations simulate the flow that develops inside a cold-gas experimental setup; the experimental setup has been previously described by Vetel et al.[19] and Couton et al.,[20] where the main features of the experimental results are explored. Second, the simultaneous presence of the two vortex shedding phenomena is studied, and the numerical results are compared to the experimental ones. Finally, turbulent calculations using a classical q–ω model are presented to estimate the turbulent influence on the whole flow organization. Because several authors put forward the sensitive effect of the injected turbulence at the porous wall, its influence is taken into account, and several σ_w levels up to 10% are considered.

II. Theoretical Analysis

A. Numerical Approach

The average compressible Navier–Stokes and energy equations are solved in a Cartesian co-ordinate system on a two-dimensional grid. The grid is based on the geometry of a cold-gas simulation of Ariane 5 solid propellant rocket motors, and is dedicated to the study of self-sustained oscillations. The flow is induced by wall mass transfer through porous walls inside a confined chamber (Fig. 1). The internal geometry is mainly characterized by the presence of two injecting blocks separated by an emerging obstacle. This obstacle restricts 32% of the area of passage through the chamber. Acoustic isolation of the chamber from the exterior environment is ensured by a nozzle located at the rear end, which runs under sonic conditions during tests. To take into account all of these characteristics, the calculations were performed using a nonstructured mesh including 53,564 grid points. Special care was taken to increase the number of cells near the injecting walls and in the wake of the emerging obstacle, as well as around the nozzle. The coarsest grid was equal to 0.18×10^{-3} m, when the chamber height h_c was equal to 28×10^{-3} m. Turbulent calculations were performed considering the model q, ω of Coakley,[21] and the overall governing equations were expressed in the form

$$\frac{\partial \boldsymbol{Q}}{\partial t} + \frac{\partial \boldsymbol{F}}{\partial x_j} = \boldsymbol{K}$$

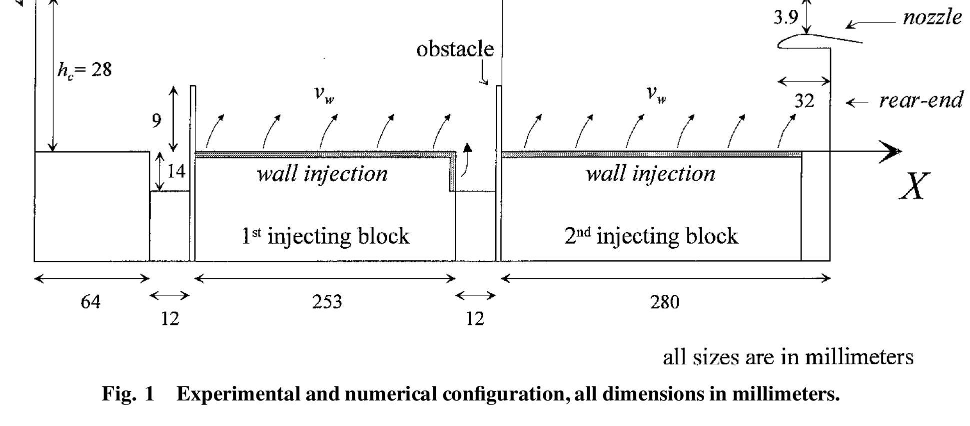

Fig. 1 Experimental and numerical configuration, all dimensions in millimeters.

where

$$\boldsymbol{Q} = \begin{pmatrix} \bar{\rho} \\ \bar{\rho}\bar{v}_i \\ \bar{\rho}\overline{E^*} \\ \bar{\rho}q \\ \bar{\rho}\omega \end{pmatrix}, \qquad \boldsymbol{F} = \begin{bmatrix} \bar{\rho}\bar{v}_j \\ \bar{\rho}\bar{v}_i\bar{v}_j + \delta_{ij}\overline{P^*} - \bar{\tau}_{ij} \\ (\bar{\rho}\overline{E^*} + \overline{P^*})\bar{v}_j - \bar{v}_i\bar{\tau}_{ij} - \lambda_T \dfrac{\partial \bar{T}}{\partial x_j} \\ \bar{\rho}q\bar{v}_j - \mu_q \dfrac{\partial q}{\partial x_j} \\ \bar{\rho}\omega\,\bar{v}_j - \mu_\omega \dfrac{\partial \omega}{\partial x_j} \end{bmatrix}$$

with the viscous terms expressed as

$$\tau_{ij} = \mu_T\left(\frac{\partial v_i}{\partial x_j} + \frac{\partial v_j}{\partial x_i}\right) - \frac{2}{3}\mu_T\delta_{ij}\left(\frac{\partial v_k}{\partial x_k}\right)$$

and $\boldsymbol{K}$ is the vector including the turbulent source terms. The λ_T total thermal conductivity and the viscosities for q and ω are expressed with the laminar and turbulent dynamic viscosities and the Prandtl numbers as follows:

$$\lambda_T = c_p(\mu/Pr + \mu_t/Pr_t)$$

$$\mu_q = \mu + \mu_t/Pr_q, \qquad \mu_\omega = \mu + \mu_t/Pr_\omega$$

The turbulent model of Coakley[21] is based on the Boussinesq assumption, that is, the Reynolds stresses Re_{ij} is linked to the mean shear stresses as

$$Re_{ij} = \frac{2}{3}\delta_{ij}\bar{\rho}q^2 - \mu_t\left[\left(\frac{\partial \bar{v}_i}{\partial x_j} + \frac{\partial \bar{v}_j}{\partial x_i}\right) - \frac{2}{3}\delta_{ij}\left(\frac{\partial \bar{v}_k}{\partial x_k}\right)\right]$$

The finite volume technique was used to solve the conservation equations, and each variable was then calculated just at the center of each computational cell, whereas flux vectors were estimated at the cell edges using the Roe[22] approximate Rieman solver and Toumi[23] extension. Time integration was provided by a second-order Runge–Kutta explicit method.

B. Boundary Conditions and Calculation Procedure

At the head end of the chamber, no-slip and adiabatic wall conditions were used for the primitive variables. To decrease the number of cells and then to decrease the calculation time, symmetric conditions were considered in the numerical simulation while a no-slip boundary condition was forced by the presence of an upper wall in the experimental setup. In fact, experimental results[24] were used to characterize the boundary layer that is established along the upper wall and the latter organizes as a stop point boundary layer with a positive pressure gradient, that is, its thickness remains at a constant level under the height of 10^{-3} m. Numerical results were found to be insensitive to the effect of the boundary layer. Flow injection through porous walls was treated like subsonic inlet conditions:

$$\dot{m}_w = c_1, \qquad p/(\gamma - 1) + \tfrac{1}{2}\rho\left(v_i^2\right) = c_2$$

$$q_w = \sigma_w v_w, \qquad \nabla\omega \,.\, \boldsymbol{n}_w = 0$$

where c_1 and c_2 are constants fixed by the experimental conditions. Because the $\dot{m}_w$ mass flow rate per injecting surface unit was fixed, v_w was derived from the latter through the perfect gas law. Note that no damping function was introduced in the turbulent model close to the injecting walls. In fact, Chaouat[11] demonstrated that such functions converge at 1.0 close to an injecting porous wall. At the rear end of the chamber, the presence of a sonic nozzle precluded any taking account of specific outflow boundary conditions. Table 1 details the main characteristics of the experimental setup, the flow properties, and the numerical model constants. Moreover, turbulent calculations permit precise characterization of the effect of the pseudoturbulence generated at the injecting surface. In case of the propellant combustion, the details of the hot-gas generation process are not currently understood, particularly for realistic propellant combustion. However, in the experimental setup, the porous walls isolate the flow in the chamber and implicitly introduce microjets, which, when merging all together, induce spatial variations in the injection velocity. Even if this pseudo-turbulence notion does not bear any resemblance to that associated with the propellant combustion, it is important to take into account such a phenomenon to be able to compare cold-gas numerical and experimental results. Beddini[10] conducted numerical investigations in which the pseudoinjected turbulence ratio σ_w was found to be one of the most important parameters in turbulent flowfield calculations. Liou et al.[12] introduced the parameter into a large-eddy simulation (LES) of a flow induced by wall mass transfer and emphasized its strong influence on flow transition. The influence of σ_w from 0 to 30% was studied by the authors. However, in a cold-gas experiment, such high levels do not sound very realistic, and Couton et al.[25] presented σ_w levels between 1 and 5%. To characterize its influence, present turbulent calculations were performed taking into account different pseudoturbulent levels at the injecting porous walls. The numerical results presented in this work were obtained both with and without turbulent model assumptions, and as regards turbulent calculations, σ_w levels were studied from 0 to 10%.

Table 1 Characteristics of experimental and numerical configuration

Flow properties		Numerical constants	
Property	Value	Constant	Value
T	298 K	C_μ	0.09
$\dot{m}_w$	2.482 kg/m^2 · s	Pr_t	0.9
Re_c	71,000	Pr_q	1
Re_w	3,700	Pr_ω	1.3
f_{1L}	278 Hz	——	——
f_{2L}	556 Hz	——	——

Each calculation was initiated with a fixed level of the Courant–Friedrich–Lewy number equal to 0.8 to guarantee numerical stability and to advance numerical results with time. These initializations were performed over 100,000 time-step iterations and were enough to obtain asymptotic converged simulations. Then, a temporal time step of 2×10^{-7} s was applied over 500,000 iterations to obtain the characterization of the flowfield in the whole chamber.

III. Flow Characterization

A. Mean and Unsteady Behavior

To characterize the flowfield, mean longitudinal velocity profiles were obtained by averaging in time results from the Navier–Stokes calculations of without-turbulence model over 100,000 iterations, simulating 100 ms of the flowfield. Figure 2 shows the specific organization of the flow; the computed mean velocity profiles throughout the whole chamber, normalized by the maximum velocity in each section, are compared with the experimental data measured by Vetel et al.[19] Upstream from the obstacle, the computed data fits perfectly with the experimental data, and profiles agree with the Taylor's classical analytical profiles (see Ref. 26) obtained for a chamber geometry free of discontinuities. This result demonstrates that there is still a laminar regime in spite of axial, Re_c and wall injection, Re_w, Reynolds numbers of high values in this region. These results confirm the laminar flow solution also observed by Majdalani and Van Moorhem[27] and Zhou and Majdalani.[28]

The presence of an emerging obstacle generates a strong perturbation in the flow, and a shear layer develops from the top of the obstacle. Some slight differences can be observed between numerical and experimental profiles in the wake of the obstacle, as well as in the region close to the injecting wall. First, as noticed by Vetel et al.,[19] experimental measurements with two-velocity component hot-wire anemometers were difficult to perform close to the injecting walls because the flow velocity is small in amplitude and changes rapidly in direction. Second, the flow can be totally disturbed by the

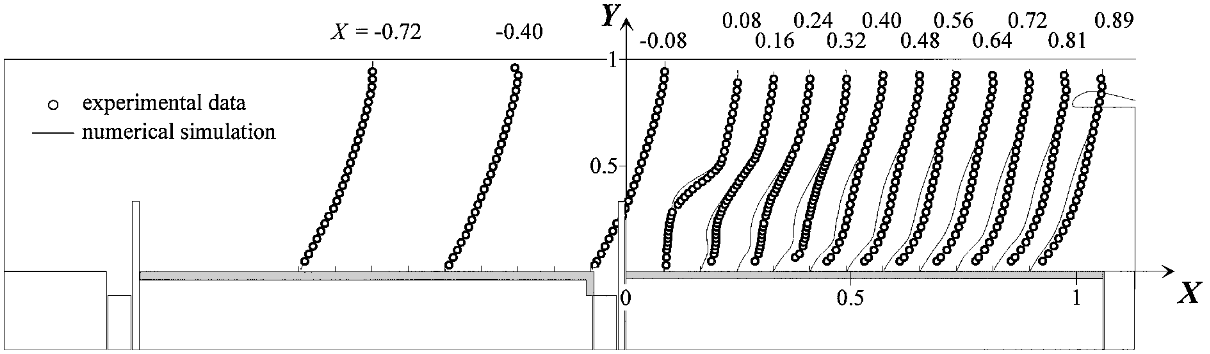

Fig. 2 Normalized axial mean-velocity profiles at various axial stations and comparison with experimental data.

emerging obstacle and can develop toward a more turbulent regime that a laminar flow simulation would not be able to reproduce quantitatively. Nevertheless, note that both experimental and numerical profiles have the same shape and provide significant transversal velocity gradients as well as inflexion points. Particularly, calculated velocity profiles show a strong disturbance close to the injecting walls. The influence of such perturbations in the flow behavior will be discussed later. The presence of inflexion points on mean velocity profiles denotes the unstable nature of the internal flow.

To evaluate the unsteady organization of the flow, the complete flowfield variables are stored at regular intervals of 2.0×10^{-4} s, and the vorticity field Ω is computed over the whole domain. Figure 3 presents several vorticity maps as a function of time downstream from the obstacle location. The change in isovorticity lines confirms the earlier noted assumption; downstream from the obstacle location, the nature of the flow is altogether unsteady. Structures are created in the wake of the obstacle and convected by the flow up until the nozzle exit. At $t = t_0$, two vortex structures $(0.1 < X < 0.2)$ are convected quite close to each other and merge at $X \approx 0.3$ in a rotational movement; this pairing is clearly observed at $t = t_3$ and provides a larger vortex structure. However, the pairing locations are not fixed in space for all vortices. For instance, two other structures located at $t = t_0$ between $X = 0.25$ and $X = 0.45$ merge at $t = t_5$ in the rear end of the chamber, whereas the two vortices developing close to the $X = 0.1$ location at $t = t_2$ merge rapidly around $X = 0.2$ at $t = t_5$. The instantaneous vorticity field also shows another strong unsteady behavior with elongated vorticity regions clearly observed in the vicinity of the injecting wall. The wall flow is then characterized by near-wall large-scale coherent structures inclined at an opposite angle compared with the mean flow direction. Indeed, experimental results demonstrated the simultaneous presence of shear layer and wall vortex shedding. As can be seen, numerical simulation may capture the two types of hydrodynamic instability, which was previously put into evidence by Traineau et al.[15] It is also interesting to quote the LES computations conducted by Venugopal et al.[29]; they obtained needle-shaped vortical structures that develop along an injecting wall in a chamber without geometric disparities. This particular shape in the vorticity field was the same as observed in the present work, as well as by Lupoglazoff and Vuillot[14] and Avalon et al.[9]

The overall coherent structures are then convected in the flow until they reach the submerged nozzle and impinge on it. In such a configuration, a coupling phenomenon between the dynamics of the flow and the acoustics can occur. This complex mechanism was also observed in both confined and open spaces, as were the impact of a circular jet on an edge, the impingement of vorticity concentrations on a corner, and the oscillations induced by flows over cavities. Ho and Nosseir[30] used a high-speed subsonic jet impinging on a flat plate to highlight the presence of a feedback loop phenomenon. This feedback loop consists of downstream convected coherent structures and upstream propagating pressure waves generated by the impingement of coherent structures on the plate. The upstream propagating waves excite the thin shear layer near the nozzle lip and produce periodic coherent structures. Dunlap and Brown[6] studied shear layer oscillations in a confined area containing sets of baffles and commented on the effect of nonlinear resonant energy transfer. Furthermore, oscillation frequency strongly depends on the Strouhal number. In addition to the critical Strouhal number, the position of the vortex separation relative to the acoustic mode structure is an important parameter with regard to the acoustic velocity node or velocity antinode. To determine whether or not a coupling behavior may occur, it is necessary to analyze closely the unsteady pressure and the velocity fluctuations in the wake of the obstacle, as well as in the vicinity of the injecting wall.

B. Vortex Shedding Phenomena

In Fig. 4, numerical spectra of the u' longitudinal fluctuating velocity component obtained at different locations in the wake of the obstacle are shown. Spectra were calculated from unsteady signals recorded during 0.1 s of simulation, and resolution of the fast Fourier transform reached 10.0 Hz. First, velocity signal close to the top of the obstacle (location 1) is mainly close to 530 Hz; the spectral response is also dominated by two other low-amplitude thin peaks located at 290 and 820 Hz. The same characteristic frequencies are also present at location 2. However, the spectral response changes rapidly with increasing distance from the obstacle position. At location 3, the energy contained at $f = 530$ Hz decreases, whereas the peak at $f = 290$ Hz becomes the dominant frequency with simultaneous strong amplification at $f = 240$ Hz. This trend is confirmed at location 4, where the 530-Hz frequency has disappeared in the velocity spectrum. Beyond this longitudinal location and in the wake of the obstacle (locations 5–7), spectral response does not noticeably change; the spectra are mainly dominated by the two frequencies of 240 and 290 Hz.

Thus, as already observed in the vorticity fields, the longitudinal evolution of velocity spectra shows that pairing processes occur in the shear layer between separation and impingement. Vortices first develop at a frequency $f = 530$ Hz, and a merging appearance results in the amplification of two peaks at $f = 240$ and 290 Hz. The latter frequency and the 530-Hz frequency are actually close to the first two theoretical acoustic modes of the chamber (Table 1). When a closed–closed cavity is considered, the nth longitudinal acoustic mode f_{nL} is based on the length L corresponding to the distance between the head end and the longitudinal location at which the nozzle condition is sonic. Therefore, this result underlines that vortex shedding is modulated at the top of the obstacle by the acoustics of the chamber. However, the presence of the second peak at $f = 240$ Hz is not linked to any acoustic mode.

To complete the spectral analysis of the fluctuating flow, the spectral organization of the longitudinal velocity component close to the injecting wall (locations 8–12) are given in Fig. 5. As mentioned before, disturbances on the mean longitudinal velocity profiles were detected; they correspond to wall structure development. Their characteristic frequencies are mainly centered at 240 and 290 Hz all along the porous wall. In the first part of the injecting block (locations 8–10), the 290-Hz frequency dominates the spectra, whereas in the rear end of the chamber (locations 11 and 12), wall

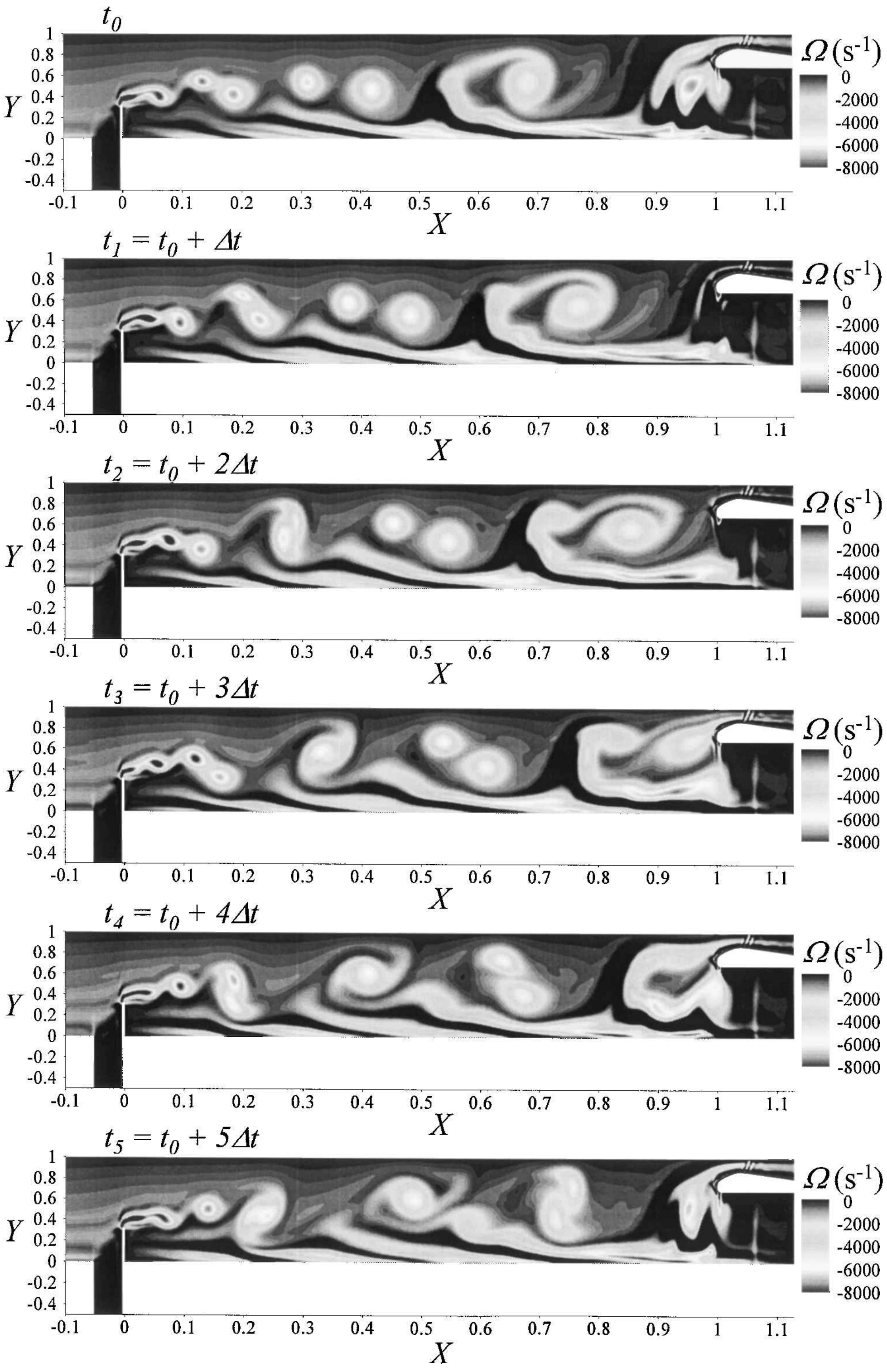

Fig. 3 Vorticity maps for the laminar calculation with $\Delta t = 0.2$ ms.

velocity fluctuations organize mainly around $f = 240$ Hz. Therefore, it can be seen that characteristic frequencies of wall vortex shedding are similar to those observed in the shear layer downstream from the pairing process location. The presence of the f_{1L} mode in the wall vortex development also demonstrates the receptivity of wall velocity fluctuations to the acoustics of the chamber. Under these conditions, both hydrodynamic instabilities can represent a source of acoustic energy by vortex–nozzle impingement. To verify this assumption, specific experimental measurements were performed in the chamber. A hot wire was located at ($X = 0.80$, $Y = 0.07$), that is, directly in the region where wall vortex shedding was numerically observed. The obtained signal was correlated with the pressure signal recorded at the head end. The calculation of the $R_{u'p'}(\tau)$ time correlation coefficient obtained (Fig. 6a) is characterized by a trigonometric shape due to acoustic frequency interaction and shows a positive time delay at which the two signals are highly correlated. According to Vetel et al.,[19] who established an analytical model able to estimate the change in correlation time, the time with the highest correlation coefficient corresponds to the delay for a wall vortex structure to convect from the velocity probe to the

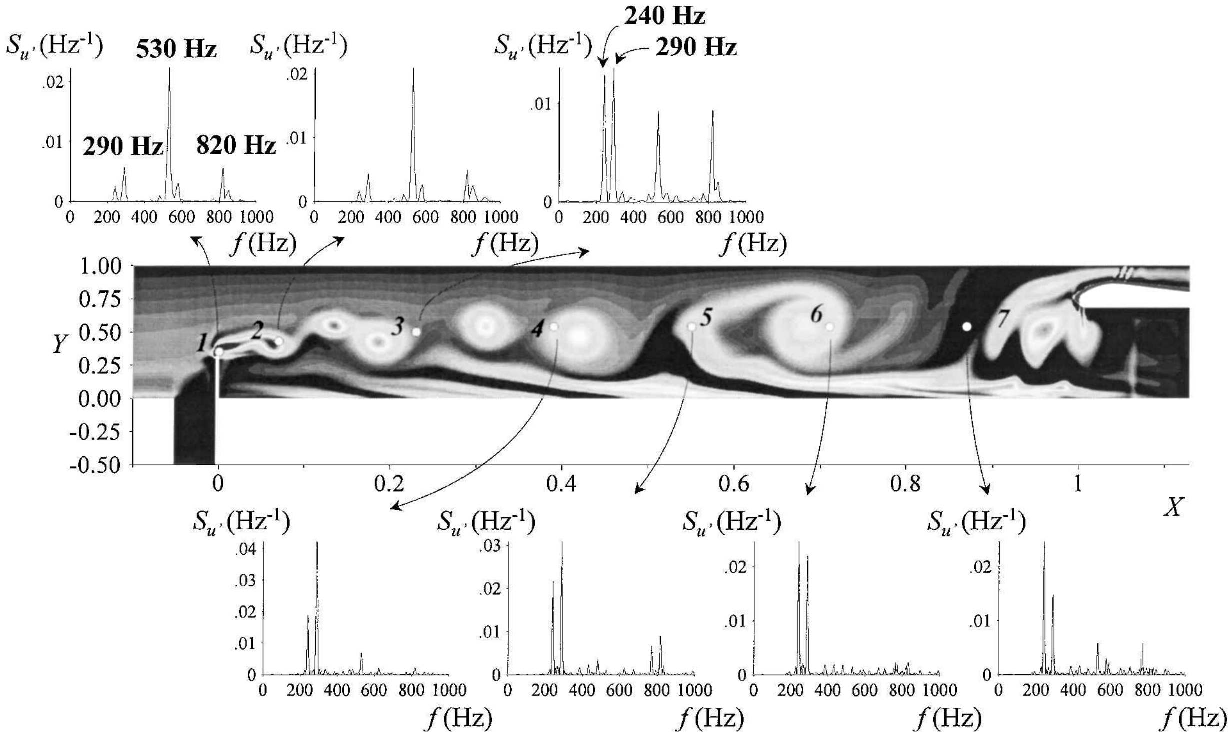

Fig. 4 Shear layer normalized power spectrum of axial velocity fluctuations at various characteristic locations.

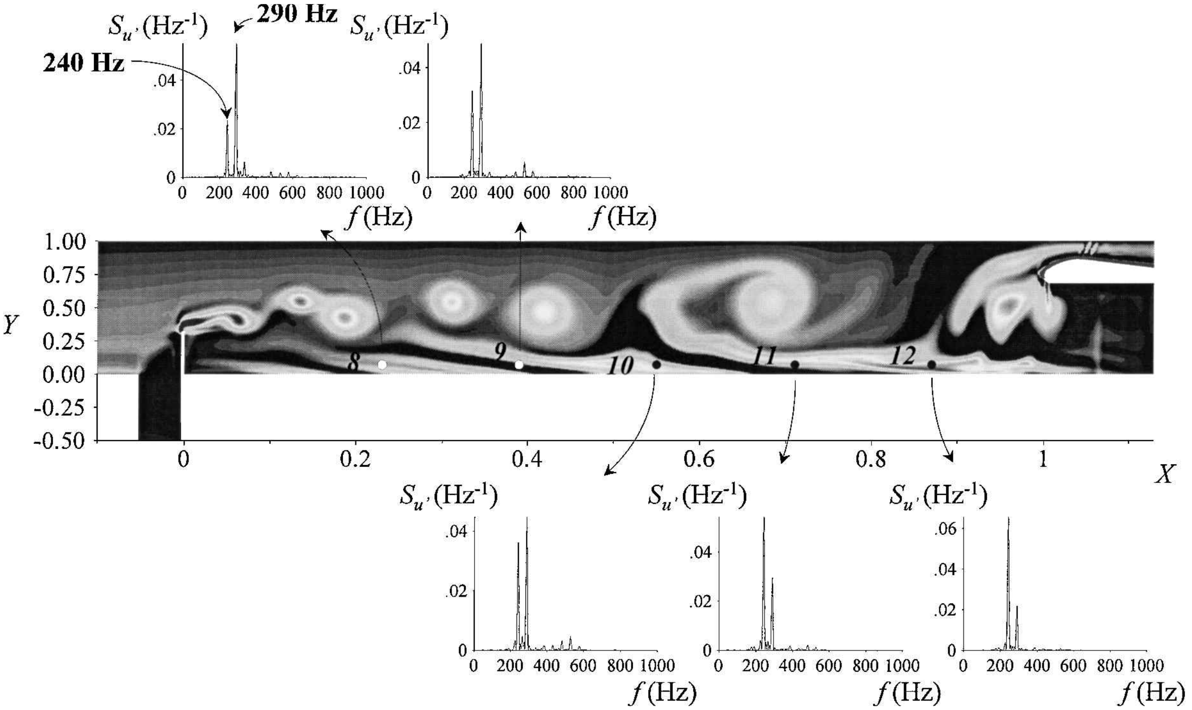

Fig. 5 Near-wall normalized power spectrum of axial velocity fluctuations at various X along $Y = 0.07$.

nozzle location and the delay for the resulting acoustic wave to travel back to the head end. After that, experimental and numerical results agree that the wall vortex shedding phenomenon acts as a strong unstable source in the flow. Therefore, the direct consequences of the unstable flow behavior can be seen in Fig. 6b, which compares the spectral pressure response at the head end between experiment and calculations. As already stated, satisfactory agreement is obtained because oscillation frequencies are correctly estimated. The experimental spectrum mainly presents two dominating peaks at 280 and 520 Hz; the latter were identified to correspond to the first and the second longitudinal acoustic modes, respectively. With the 10-Hz accuracy in the numerical spectral response, the acoustic modes of the chamber are well reproduced. The experimental spectrum provides a large band frequency including frequencies from 230 to 290 Hz, with a low-level emerging peak close to 240 Hz. However, numerical results show that the 240-Hz frequency is the dominant energy peak in the pressure fluctuation signal. To identify the meaning of this frequency, additional comparisons have to be made.

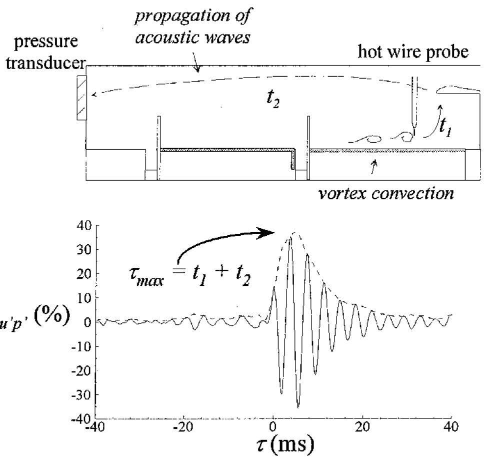

Fig. 6a $R_{u'p'}(\tau)$ correlation coefficient between velocity fluctuations measured at ($X = 0.80$, $Y = 0.07$) and pressure oscillations recorded at the head end.

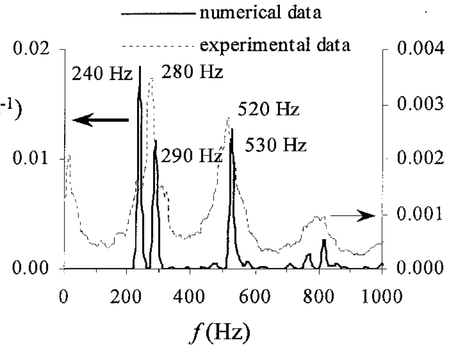

Fig. 6b Spectra of pressure oscillations at head end from both computed and experimental results.

The spectral response of velocity fluctuations in three different characteristic locations is presented in Fig. 7. The first is located close to the shear layer separation. Experimental results underline two main emerging frequencies. The frequency of 450 Hz was found to be a natural unstable frequency of the shear layer, and the frequency of 280 Hz is a response of the shear layer to the acoustics as also predicted by numerical results. For location 2, both numerical and experimental results show vortex merging resulting in a decrease of the fluctuation frequencies. However, the velocity spectrum issuing from experiment is also characterized by the presence of the f_{1L} mode, whereas the numerical case shows a high level of energy around $f = 240$ Hz. Finally, location 3 reveals the most significant discrepancy between numerical and experimental results. Indeed, the wall vortex shedding frequencies are charaterized by a broadband spectrum around a natural frequency of 480 Hz, whereas numerical calculation estimates coherent structures shedding frequencies of a well-organized flow pattern at $f = 240$ and 290 Hz. Furthermore, the experimental response is dominated by a turbulent behavior to such a point that wall velocity fluctuations do not show a strong receptivity to pressure oscillations because the f_{1L} mode does not emerge in the spectrum. Because Beddini[10] insisted on the influence of pseudoturbulent levels due to the injecting condition through porous wall, turbulent calculations were performed.

C. Turbulent Simulations

Turbulent calculations were effected taking into account the pseudoinjected turbulence phenomenon. Given that boundary conditions were modified at wall injection through the σ_w level, the spectra of the fluctuating velocity close to the porous wall are presented in Fig. 8 to estimate flow modifications. Whereas laminar calculations showed the presence of dominant frequencies close to 240 and 290 Hz, it can be seen that the same unsteady behavior is observed with the turbulent model for the $\sigma_w = 0$ case. However, by the increase of the pseudoinjected turbulence level to $\sigma_w = 2.5\%$, different wall vortex shedding behavior appears. First, spectra are characterized by other frequencies, that is, $f = 225$, 450, and 675 Hz; the level depends on longitudinal location. Second, no velocity fluctuation energy is concentrated around the f_{1L} mode. For the last σ_w

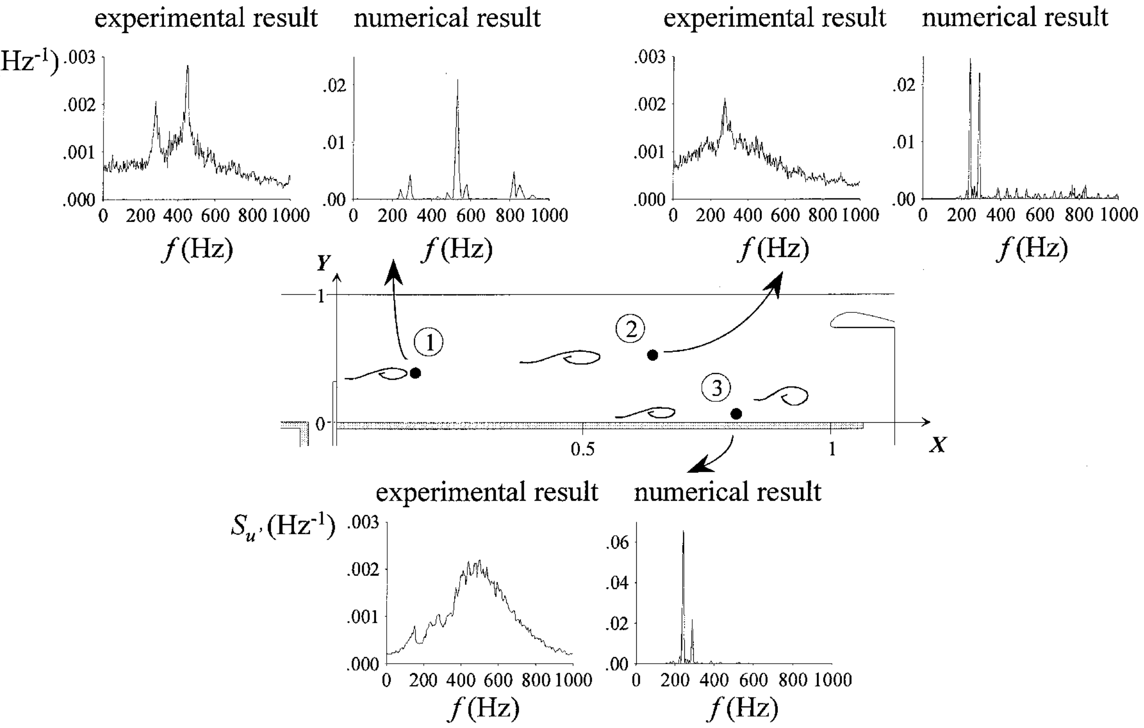

Fig. 7 Comparison between numerical and experimental spectra of axial velocity fluctuations at two locations inside the shear layer and near porous wall.

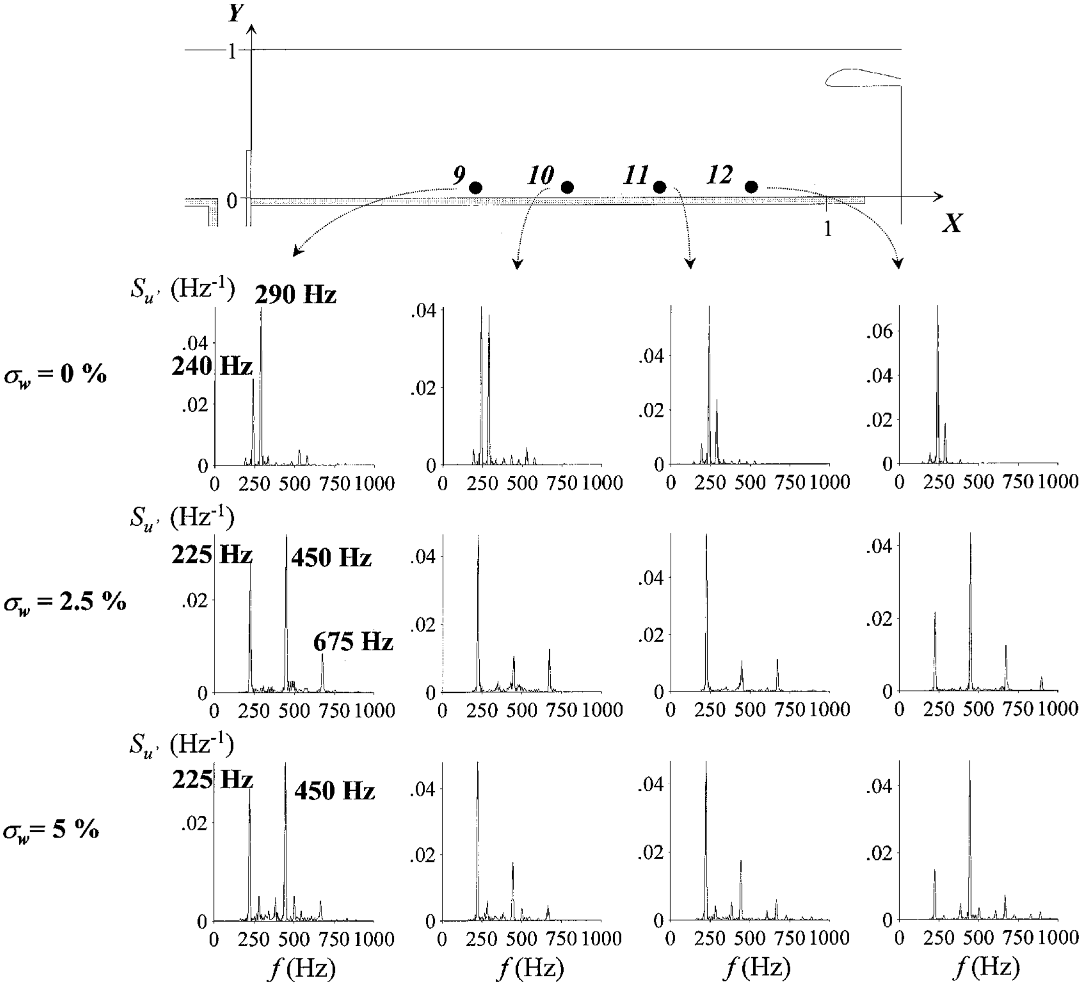

Fig. 8 Influence of turbulent calculations and wall pseudoturbulence levels on the spectral organization in the flow near porous wall.

presented ($\sigma_w = 5\%$), this trend is confirmed; wall vortex are shed at two frequencies ($f = 225$ and 450 Hz). Thus, the unsteady behavior of the flow appears to be strongly affected by the level of σ_w. Figure 9, where the pressure spectra at head end is plotted for $\sigma_w = 5\%$, supports this. Pressure fluctuations are dominated by two peaks at $f = 225$ and 450 Hz, related to the wall velocity fluctuations' characteristic frequencies. In other words, with the disappearance of the f_{1L} mode in pressure spectra, no resonance phenomenon is observed.

These results provide important information on the flowfield organization. On the one hand, by introducing a pseudoinjected turbulence level at the porous wall, the receptivity of wall velocity fluctuations to pressure oscillations is weakened; this result was also observed in the experimental work. On the other hand, because the wall velocity fluctuations are sensitive to σ_w levels, the 225 and 450 Hz frequencies are the characteristic shedding frequencies of wall vortices. The 450-Hz frequency is actually close to the experimental frequency of 480 Hz and corresponds to the first harmonic of the 225-Hz frequency. Under such conditions, the interaction between the two unstable sources is clearly demonstrated. Wall vortices are driven by a hydrodynamic frequency and develop along the porous wall until the rear end of the chamber. The vortex–nozzle interaction generates acoustic pressure oscillations that directly influence shear layer vortex shedding at the top of the obstacle. Therefore, wall instability represents the dominant source of acoustic energy in the flow, which is also the conclusion of experimental investigations.[15] Thus, in this kind of flow configuration, the pressure field is able to act on the shear layer vortex shedding and to generate self-sustained oscillations. However, the influence of pressure oscillations on the wall vortex shedding is weakened by the pseudoinjected turbulence. In this case, wall instability is responsible for pressure wave generation without self-sustained oscillations occurring.

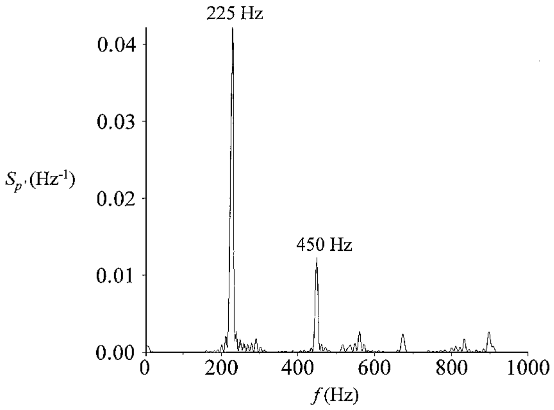

Fig. 9 Normalized power spectrum of pressure fluctuations at head end for $\sigma_w = 2.5\%$.

It would be interesting to understand why this wall instability has a stronger influence on pressure oscillations than does shear layer instability. In Fig. 10, the change of the It turbulence intensity profiles at different locations downstream from the obstacle location is shown. Experimental results, It_{exp}, are compared with levels computed from the q turbulent velocity field with σ_w equal to 0% as well as levels of It estimated from the time-dependent velocity field, It_{num}, and several trends are underscored. The first confirmed that the shear layer is turbulent whatever the longitudinal location may be, with a characteristic peak of q directly at the height of the

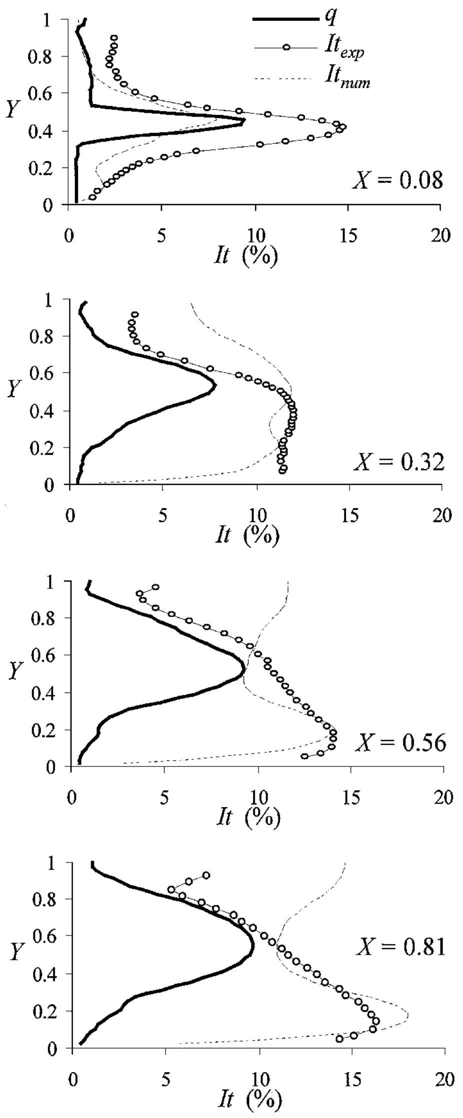

Fig. 10 Computed turbulence intensity profiles at four locations downstream from the obstacle location and comparison with experiment, $\sigma_w = 0$.

top of the obstacle. Therefore, turbulence in the wake of the obstacle acts as a dissipation source that weakens coupling between the shear layer vortex shedding and the acoustics. However, turbulence is weak in the vicinity of the injecting walls; coherent wall vortices are favored by high-velocity fluctuation levels. Thus, the flow is unsteady and mainly organizes in a laminar way, which explains why wall vortex–nozzle interaction is significant.

Finally, Table 2 shows the influence of the different simulations involved on the overall pressure oscillation level. For the laminar case, the nondimensional pressure fluctuation rms reaches 10 times the one obtained in the experimental case, but this value is strongly affected by turbulent simulations. For $\sigma_w = 0$, pressure $\sqrt{p'^2}/p$ is decreased to 0.19%, whereas for the $\sigma_w = 2.5\%$ case, this value is 0.084%. The high difference between these two levels of σ_w can be easily explained by that, for $\sigma_w = 2.5\%$, no resonance is observed, that is, pressure fluctuations are not organized close to an acoustic mode; then, no subsequent amplification by the confined chamber arises. For the other calculations, the higher the pseudoturbulent level is, the lower the pressure oscillation level, reaching twice the experimental value for $\sigma_w = 10\%$. However, although turbulent calculations strongly decrease the oscillatory behavior of the flow, it is evident that, when computed, unsteady pressure levels are much higher than experimental figures.

Table 2 Influence of σ_w levels on noise generation

Flow	$\sqrt{p'^2}/p$,%
Laminar	0.252
Turbulent	
$\sigma = 0\%$	0.190
$\sigma = 2.5\%$	0.084
$\sigma = 5\%$	0.070
$\sigma = 10\%$	0.055
Experiment	0.025

To understand such discrepancies, additional parameters or flow characteristics have to be taken into account. According to Lupoglazoff and Vuillot,[14] porous wall admittance could be the reason for low experimental levels. Their estimation of the acoustic mass response of the porous wall resulted in a quasi-steady law independent of the frequency:

$$\dot{m}_w = a \cdot p^n$$

where a is a constant fixed by experimental conditions. To check the influence of such boundary conditions on the flowfield behavior, a similar response was introduced in the $\sigma_w = 2.5\%$ turbulent case; the value $n = -12$, such as the one used by the authors, was found to be close to the porous wall characteristics employed in the present work. The results showed that no difference appeared in the frequencies involved in the pressure and velocity spectra compared with the case without porosity response. Nevertheless, a strong influence was observed on the overall pressure fluctuation level. The computed $\sqrt{p'^2}/p$ ratio reached 0.038%, that is, less than half that obtained without porosity response, that is, 1.5 times higher than the level obtained in the experiment. This result indicates that, for better noise-level prediction, the porous wall acoustic response must be taken into account.

IV. Conclusions

The study of a flow induced by injecting porous walls inside a confined chamber has been numerically carried out; the chamber included an emerging obstacle, as well as a submerged nozzle. This work was part of a study evaluating periodic vortex shedding as a source of acoustic energy in solid propellant rocket motors. As a result of the cold-gas model, as well as time-dependent compressible Navier–Stokes equations with- and without-turbulence models, some key conclusions may now be drawn.

First, experimental and numerical results agree that an unstable phenomenon occurs in the wake of the obstacle as a shear layer instability. Vortices are shed and impinge on the submerged nozzle. Self-sustained oscillations occur between velocity and pressure fluctuations. The shear layer, modulated by acoustics, showed in numerical simulations that nonlinear phenomena, such as pairing processes, are observed, which result in a vortex shedding frequency that matched with an acoustic mode.

Second, and by far the most important result, the role of injection through porous walls is underlined by an unstable development in the vicinity of the porous walls. Wall vortex shedding is created, and elongated vortices are convected all along the porous wall and impinge on the nozzle at the rear end of the chamber. Experimentally, this second unstable source was also detected and found to be the most important unstable source, that is, it generates the resonant state.

Finally, turbulent calculations with a classical q–ω turbulent model were used to estimate the role of the pseudoinjected turbulence on the flow organization. Turbulence acts quite particularly as a dissipation source on shear layer vortices, and the higher the pseudoturbulent levels are, the better the head-end pressure fluctuation prediction's. Furthermore, the injected pseudoturbulence levels weakened the influence of the acoustics on the wall vortex shedding, which is driven by hydrodynamic frequencies. Numerical results failed to predict pressure oscillation levels. In fact, computations taking into account the response of the porous wall were conducted and showed more satisfactory agreement. Nevertheless, even if turbulent calculations slightly improved the results obtained in comparison with the experimental ones, the unsteady flow in terms of broadband spectra was poorly reproduced. This problem is of special importance. Indeed, in the experimental work, even if the influence of pressure oscillations on wall velocity fluctuations is not observed, the wall vortex shedding frequency band is so broad that the first acoustic modes are simultaneously excited. However, with statistical turbulent models, such broadband spectra are not observed; no resonance takes place. Also note that, even if a statistical model is not adapted to such unsteady solutions, the results allow one to describe the main features occurring in this particular flow. In fact, in the wake of the obstacle, the model is able to catch the generation of the large structures while it takes into account the dissipation through turbulence. Nevertheless, the dissipation process is not entirely taken into account, which explains, for instance, the main difference of spectral response obtained between numerical and experimental results.

Because of the improvement of unsteady turbulent models such as LES, three-dimensional numerical simulations should entail better flow prediction. From a fundamental point of view, such simulations should also provide further information on this complex flow. For instance, experimental results showed that shear layer and wall vortex shedding are characterized by hydrodynamic frequencies very close to each other. The presence of a sheared flow is probably the destabilization effect responsible for the wall instability appearance. The links between the two instabilities, that is, the shear layer with the wall vortices interaction and the energy transfer between them, have yet to be fully understood. It also will be interesting to provide spatial-dependent conditions at the injecting wall to characterize their influence on the vortex shedding phenomena.

Acknowledgments

This research was sponsored by the Centre National d'Etudes Spatiales (CNES). We wish to give special thanks to Michel Pons, director of the Solid Propulsion Department, for his tireless aid. These studies were performed within the framework of the Aerodynamics of Solid Segmented Motors research program of CNES, concerning the MPS/P230 of Ariane 5, and as a result of a research agreement with the Office National d'Etudes et de Recherches Aérospatiales.

References

[1] Mathes, H. B., "Assessment of Chamber Pressure Oscillations in Shuttle Solid Rocket Booster Motor," 16th AIAA/SAE/ASME, Hartdord Connecticut, June 30-July 2, 1980, pp. 1–10.

[2] Blomshield, F. S., and Mathes, H. B., "Pressure Oscillations in Post-Challenger Space Shuttle Redesigned Solid Rocket Motors," *Journal of Propulsion and Power*, Vol. 9, No. 2, 1993, pp. 217–221.

[3] Scippa, S., Pascal, P., and Zanier, F., "Ariane 5 MPS Chamber Pressure Oscillations Full Scale Firings Results Analysis and Further Studies," 30th AIAA/ASME/SAE/ASEE Joint Propulsion Conf., Indianapolis, IN, June 1994.

[4] Flandro, G. A., "Vortex Driven Mechanism in Oscillatory Rocket Flows," *Journal of Propulsion and Power*, Vol. 2, No. 3, 1986, pp. 206–214.

[5] Vuillot, F., "Vortex Shedding Phenomena in Solid Rocket Motors," *Journal of Propulsion and Power*, Vol. 11, No. 4, 1995, pp. 626–639.

[6] Dunlap, R., and Brown, R. S., "Exploratory Experiments on Acoustic Oscillations Driven by Periodic Vortex Shedding," *AIAA Journal*, Vol. 19, No. 3, 1981, pp. 408, 409.

[7] Brown, R. S., Dunlap, R., Young, S. W., and Waugh, R. C., "Vortex Shedding as a Source of Acoustic Energy in Segmented Solid Rockets," *Journal of Spacecraft and Rockets*, Vol. 18, No. 4, 1981, pp. 312–319.

[8] Yeh, Y. P., Heaman, J. P., Ramachandran, N., and Smith, A. W., "Subscale Cold Gas Flow Simulation of the Port Flow in Solid Rocket Motors," 30th AIAA/ASME/SAE/ASEE Joint Propulsion Conf., Indianapolis, IN, June 1994.

[9] Avalon, G., Casalis, G., and Griffond, J., "Flow Instabilities and Acoustic Resonance of Channels with Wall Injection," 34th AIAA/ASME/SAE/ASEE Joint Propulsion Conf. and Exibit, Cleveland, OH, July 1998.

[10] Beddini, A. R., "Analysis of Injection Induced Flows in Porous Walled Duct with Application to Aerochemistry of Solid Propellant Motor," Ph.D. Dissertation, Mechanical and Aerospace Engineering, Rutgers Univ., New Brunswick, NJ, Oct. 1981.

[11] Chaouat, B., "Flow Analysis of a Solid Propellant Rocket Motor with Aft Fins," *Journal of Propulsion and Power*, Vol. 13, No. 2, 1997, pp. 194–196.

[12] Liou, T. M., Lien, W. Y., and Hwang, P. W., "Transition Characteristics of Flowfield in a Simulated Solid-Rocket Motor," *Journal of Propulsion and Power*, Vol. 14, No. 3, 1998, pp. 282–289.

[13] Dunlap, R., Blackner, A. M., Waugh, R. C., Brown, R. S., and Willoughby, P., "Internal Flowfield Studies in a Simulated Cylindrical Port Rocket Chamber," *Journal of Propulsion and Power*, Vol. 6, No. 6, 1990, pp. 690–704.

[14] Lupoglazoff, N., and Vuillot, F., "Numerical Simulations of Parietal Vortex-Shedding Phenomenon in a Cold Flow Setup," 34th AIAA/ASME/SAE/ASEE Joint Propulsion Conf. and Exibit, Cleveland, OH, July 1998.

[15] Traineau, J. C., Prevost, M., Vuillot, F., Le Breton, P., Cuny, J., Preioni, N., and Bec, R., "A Subscale Test Program to Assess the Vortex Shedding Driven Instabilities in Segmented Solid Rocket Motors," 33rd AIAA/ASME/SAE/ASEE, Seattle, WA, July 1994.

[16] Dotson, K. W., Koshigoe, S., and Pace, K. K., "Vortex Shedding in a Large Solid Rocket Motor Without Inhibitors at the Segment Interfaces," *Journal of Propulsion Power*, Vol. 13, No. 2, 1997, pp. 197–206.

[17] Zhao, Q., Staab, P. L., Kassoy, D. R., and Kirkkopru, K., "Acoustically Generated Vorticity in an Internal Flow," *Journal of Fluid Mechanics*, Vol. 413, 2000, pp. 247–285.

[18] Staab, P. L., Zhao, Q., Kassoy, D. R., and Kirkkopru, K., "Co-existing Acoustic-Rotational Flow in a Cylinder with Axisymmetric Sidewall Mass Addition," *Physics of Fluids*, Vol. 11, 1999, pp. 2935–2951.

[19] Vetel, J., Plourde, F., and Doan-Kim, S., "Mixing Effects Between Self-Sustained Oscillations and Unstable Hydrodynamic Behavior near Injecting Walls," *AIAA Journal*, Vol. 39, No. 8, 2001, pp. 1455–1468.

[20] Couton, D., Plourde, F., and Doan-Kim, S., "Cold-Gas Simulation of a Solid Propellant Rocket Motor," *AIAA Journal*, Vol. 34, No. 4, 1996, pp. 2514–2522.

[21] Coakley, T. J., "Turbulence Modelling Methods for Compressible Navier–Stokes Equations," 16th AIAA Fluid and Plasma Dynamics Conf., Denvers, MA, June 1983.

[22] Roe, P. L., "Approximate Riemann Solvers, Parameter Vectors and Difference Schemes," *Journal of Computational Physics*, Vol. 43, 1981, pp. 357–372.

[23] Toumi, I., "A Weak Formulation of Roe's Approximate Solver," *Journal of Computational Physics*, Vol. 102, No. 2, 1992, pp. 360–373.

[24] Plourde, F., Poisson, R., and Doan-Kim, S., "Space Correlation Measurements in a Forced Shear-Layer with Wall Injection," *Experiments in Fluids*, Vol. 21, No. 1, 1996, pp. 26–32.

[25] Couton, D., Doan-Kim, S., Vuillot, F., "Numerical Simulation of Vortex-Shedding Phenomenon in a Channel with Flow Induced Through Porous Wall," *International of Journal Heat and Fluid Flow*, Vol. 18, No. 3, 1997, pp. 283–296.

[26] Taylor, S. G., "Fluid Flow in Regions Bounded by Porous Surface," *Proceedings of the Royal Society of London, Series A: Mathematical and Physical Sciences*, Vol. 232, No. 1199, 1956, pp. 456–475.

[27] Majdalani, J., and Van Moorhem, W. K., "Improved Time-Dependant Flowfield Solution for Solid Rocket Motors," *AIAA Journal*, Vol. 36, No. 2, 1998, pp. 241–248.

[28] Zhou, C., and Majdalani, J., "Improved Mean Flow Solution for Slab Rocket Motros with Regressing Walls," *Journal of Propulsion and Power*, Vol. 18, No. 3, 2002, pp. 703–711.

[29] Venugopal, P., Najjar, F. M., and Moser, R. D., "DNS and LES Computations of Model Solid Rocket Motors," 30th AIAA/ASME/SAE/ASEE Joint Propulsion Conf. and Exibit, Hunstville, AL, July 2000.

[30] Ho, C. M., and Nosseir, N. S., "Dynamics of an Impinging Jet. Part 1: The Feedback Phenomenon," *Journal of Fluid Mechanics*, Vol. 105, 1981, pp. 119–142.